Unresolved stochastic background from compact binary mergers detectable by next-generation ground-based gravitational-wave observatories

Darsan S. Bellie,[1,2,*] Sharan Banagiri,[1] Zoheyr Doctor,[1,2] and Vicky Kalogera[1,2]

[1]*Center for Interdisciplinary Exploration and Research in Astrophysics (CIERA), Northwestern University, 1800 Sherman Avenue, Evanston, Illinois 60201, USA*

[2]*Department of Physics and Astronomy, Northwestern University, 2145 Sheridan Road, Evanston, Illinois 60201, USA*

(Received 13 October 2023; accepted 18 April 2024; published 8 July 2024)

The next generation of ground-based gravitational-wave detectors will look much deeper into the Universe and have unprecedented sensitivities and low-frequency capabilities. Especially alluring is the possibility of detecting an early-Universe cosmological stochastic background that could provide important insights into the beginnings of our Universe and fundamental physics at extremely high energies. However, even if next-generation detectors are sensitive to cosmological stochastic backgrounds, they will be masked by more dominant astrophysical backgrounds, namely the residual background from the imperfect subtraction of resolvable compact binary coalescences (CBCs) as well as the CBC background from individually unresolvable CBCs. Using our latest knowledge of masses, rates, and delay time distributions, we present a data-driven estimate of the unresolvable CBC background that will be seen by next-generation detectors. Accounting for statistical errors and astrophysical systematics, this estimate quantifies an important piece in the CBC noise budget for next-generation detectors and can help inform detector design and subtraction algorithms. Importantly, we find that the neutron-star black-hole binary contribution to the unresolved CBC background is further comparable to the binary neutron star contribution. We compare our results with predictions for backgrounds from several cosmological sources in the literature, finding that the unresolvable background will likely be a significant impediment for many models. This motivates the need for simultaneous inference methods or other statistical techniques to detect early-Universe cosmological backgrounds.

DOI: 10.1103/PhysRevD.110.023006

I. INTRODUCTION

In 2015, the Laser Interferometer Gravitational-Wave Observatory (LIGO) [1] directly detected gravitational waves (GWs) for the first time by capturing the coalescence of two stellar-mass binary black holes (BBHs) [2]. This was eventually followed by the detection of GWs from binary neutron stars (BNSs) [3] and neutron-star black-hole binaries (NSBHs) [4] by the LIGO and Virgo observatories [5]. Constituting the category of compact binary coalescences (CBCs), these sources have heralded the arrival of GW astronomy with nearly a hundred detected candidates already [6–8].

While we have only detected GWs from CBCs so far, several other sources have been theorized and expected. In particular, several models postulate the presence of "cosmological" GWs, predominantly showing up as a cosmological stochastic gravitational wave background (SGWB) [9–11]. These might be accessible by next-generation ground-based GW detectors (henceforth known as XG detectors) like Cosmic Explorer (CE) and Einstein Telescope (ET) [12–19]. Cosmological SGWBs originating from the early Universe might carry imprints of the physics of the earliest epochs in the Universe, inaccessible through any other channels. Detection of such a background would therefore drastically expand our understanding of the first instants in the Universe and unlock fundamental physics at very high energies well beyond the reach of particle accelerators [9].

However, such cosmological SGWBs can be shielded by the GWs arising from various astrophysical sources [20–22] and in particular CBCs of stellar origin since they are expected to be the largest contributor to the GW power in the frequency band of XG detectors. The GWs from CBCs will pose a major challenge for the capability of XG detectors to detect cosmological backgrounds. There are two components of such astrophysical shielding, coming from "resolved" and "unresolved" CBCs. Resolved sources, here, refer to those sources with GW signals that can be individually and confidently detected within the detector noise.

The proposed XG detectors are expected to have a high redshift reach to astrophysical CBC sources owing to their

*darsh@northwestern.edu

better sensitivities and low-frequency capabilities of ∼2 or 3 Hz[1] [12–16,24,25]. It is expected that XG detectors would be able to resolve nearly all BBHs of stellar origin in the Universe as well as many BNSs and NSBHs up to redshifts of a few [12–16]. To minimize their impact on searches for cosmological SGWBs, significant ongoing work is devoted to developing techniques to subtract resolvable CBCs from GW data [26–31]. However, the subtraction residue from imperfect subtraction could still be a challenge for XG detectors [26,27].

In addition to the resolvable CBC signals, we also expect an astrophysical SGWB originating from the incoherent superposition of unresolvable CBC sources. Such an astrophysical SGWB is a key detection target for current-generation ground-based detectors [32–34], but it can also shield cosmological SGWBs. Crucially, this unresolved CBC background represents a noise source that is independent of the fidelity and efficacy of subtraction. Accurately characterizing this background will enable us to understand the accessibility of cosmological SGWBs to XG detectors, will inform us of the necessary levels of subtraction of resolvable signals, and will provide an important data point in comparing detector designs and networks. In this paper, we provide a data-driven estimate of the unresolvable CBC SGWB for different configurations of XG detector networks, by drawing upon several empirical models that come from the population inference of LIGO-Virgo-KAGRA (LVK) GW observations and of Galactic BNSs. By utilizing multiple models, we provide robust estimates that account for both statistical and astrophysical systematic uncertainties.

The rest of the paper is organized as follows. In Sec. II we briefly motivate the paper and place our study in the context of previous literature for XG detectors. In Sec. III, we mathematically define the SGWB and describe how an astrophysical SGWB can be calculated from a set of sources. Section IV describes our assumptions on the astrophysical merger rates, mass distributions, and redshift distributions which we use to compute the unresolved background, and Sec. V describes our choices of detector network configurations. In Sec. VI, we detail our formalism to numerically compute the unresolved background from CBC sources, and in Sec. VII, we discuss the cosmological SGWB models that we use. Section VIII presents our results, and Sec. IX discusses their implications and comments on future work needed.

Throughout this paper, G is the gravitational constant, c the speed of light, H_0 the Hubble constant, and we define our cosmology using the Λ Cold Dark Matter (CDM) model with cosmological parameters taken from Planck 2018 [35].

[1]However, studies of Newtonian noise [23] show that it will be a serious impediment at frequencies below 5 Hz even at the depths of ET.

II. THE UNRESOLVED SGWB FROM CBCS

The total GW energy-density spectrum $\Omega_{\rm GW}$ as seen by a GW detector is the sum of the GW energy-density spectrum from cosmological sources $\Omega_{\rm cosmo}$ and from astrophysical sources[2] $\Omega_{\rm astro}$ [30],

$$\Omega_{\rm GW} = \Omega_{\rm astro} + \Omega_{\rm cosmo}. \tag{1}$$

In general, the astrophysical component can mask the cosmological component if $\Omega_{\rm astro} > \Omega_{\rm cosmo}$. For the rest of this paper, we assume that $\Omega_{\rm astro} = \Omega_{\rm cbc}$ and that the GW energy from other sources can be neglected so that

$$\Omega_{\rm GW} \approx \Omega_{\rm cbc} + \Omega_{\rm cosmo}. \tag{2}$$

Various methods have been developed to subtract resolvable CBC signals in order to minimize their impact on searches for $\Omega_{\rm cosmo}$ [26–31,36]. Such techniques, however, are always imperfect, as they depend on parameter estimation results and can also suffer from waveform systematics. The imperfect subtraction leaves behind a residue $\Omega_{\rm cbc,\,residue}$ that contributes to the effective SGWB from CBCs [26,30].

In addition to the resolved CBC signals, the incoherent superposition of the unresolvable CBC signals gives rise to an astrophysical SGWB that we call $\Omega_{\rm cbc,\,unres}$. Therefore, effectively,

$$\Omega_{\rm cbc} = \Omega_{\rm cbc,\,unres} + \Omega_{\rm cbc,\,residue}. \tag{3}$$

While some studies find that $\Omega_{\rm cbc,\,residue}$ remains a major challenge for detecting cosmological SGWBs [26,27], others find that $\Omega_{\rm cbc,\,unres}$ will provide the noise floor [28,29,36].[3] Since $\Omega_{\rm cbc,\,unres}$ is a purely stochastic noise, it will have to be fit simultaneously with any cosmological SGWB.

While some constraints were previously placed on $\Omega_{\rm cbc,\,unres}$ for XG detectors by Refs. [18,26,29,30,37,38] they were either limited by the dearth of data before O3, or by simple population models or both. References [26,27] in particular account for uncertainties in merger rates by using 90% credible levels, but do not incorporate the relation between the rate uncertainty and uncertainties in other model parameters. Furthermore, papers in the literature generally do not include the SGWB contribution from NSBHs, which we find is comparable with that of BNSs.[4]

[2]i.e., of stellar origin.

[3]Some caveats are in order: (i) Ref. [29] assumes in their notching analysis that the parameters of resolved signals are perfectly known, and (ii) Ref. [28] applies their method only to a small set of BBH signals with high signal-to-noise ratios.

[4]Although Ref. [38] includes NSBHs in their estimate, their estimate was not conditioned on NSBH detections.

In our study, we implement a data-driven estimate of $\Omega_{\rm cbc,\,unres}$ for XG detectors, using the latest inferences on the CBC population from LVK data. Wherever possible, we consistently incorporate the uncertainty from the rate and from the population modeling. In addition, we consider several population models to propagate the astrophysical systematic uncertainty stemming from parameterized GW analyses to present uncertainty envelopes for $\Omega_{\rm cbc,\,unres}$.

III. CALCULATING THE SGWB FROM CBCS

The SGWB from any type of GW source is generally characterized by the dimensionless GW energy-density spectrum [39]

$$\Omega_{\rm GW}(f) = \frac{f}{\rho_c}\frac{d\rho_{\rm GW}}{df}(f), \tag{4}$$

where f is the observed GW frequency, $\rho_c = 3H_0^2c^2/8\pi G$ is the critical density needed to close the Universe, and $\rho_{\rm GW}$ is the GW energy density at f.

The GW energy density $\rho_{\rm GW}$ arising from astrophysical sources is given by

$$\frac{d\rho_{\rm GW}}{df}(f) = \frac{1}{c}F(f), \tag{5}$$

where F is the GW energy flux in the observer frame [40]. We define the energy flux by summing up the individual fluxes in a population of astrophysical sources between redshifts $z_{\rm low}$ to $z_{\rm up}$ and with an associated set of source parameters θ as [20,31]

$$F(f) = \int_\theta p(\theta)d\theta \int_{z_{\rm low}}^{z_{\rm up}} \frac{dR_o(z)}{dz}\frac{\frac{dE_{\rm gw}(f_s,\theta)}{df_s}(1+z)^2}{4\pi d_L^2}dz, \tag{6}$$

where $p(\theta)$ is the distribution of the source parameters and d_L is the luminosity distance. The source-frame GW energy spectrum emitted by each astrophysical source is given by $dE_{\rm gw}(f_{\rm s},\theta)/df_{\rm s}$, where $f_{\rm s} = f(1+z)$ is the source-frame frequency.

For astrophysical sources distributed isotropically across the Universe, the rate of observed signals R_o in some redshift slice dz is

$$\begin{aligned}\frac{dR_o(z)}{dz} &= \frac{dN(z)}{dzdt_o} = \frac{dN(z)}{dV_c dt_s}\frac{dt_s}{dt_o}\frac{dV_c}{dz}(z)\\ &= R_\nu(z)\frac{1}{1+z}\frac{dV_c}{dz}(z),\end{aligned} \tag{7}$$

where N specifies the number of events occurring in a given cosmic slice and $dt_s/dt_o = 1/(1+z)$ accounts for time dilation between the source and observer. $R_\nu(z) = dN(z)/dV_c dt_s$ is the source-frame rate density per comoving volume V_c of a specific type of astrophysical source ν. The differential comoving volume element is given by [41]

$$\frac{dV_c}{dz}(z) = \frac{4\pi d_L^2}{(1+z)^2}\frac{c}{H_0E(z)}, \tag{8}$$

where, for a flat ΛCDM cosmology and ignoring radiation density, $E(z) = \sqrt{\Omega_M(1+z)^3+\Omega_\Lambda}$ [20,31]. Bringing this all together, we arrive at the energy-density spectrum for a SGWB arising from astrophysical sources distributed isotropically across the Universe between some redshifts $z_{\rm low}$ to $z_{\rm up}$:

$$\Omega_{\rm GW}(f) = \frac{f}{\rho_c H_0}\int_\theta\int_{z_{\rm low}}^{z_{\rm up}} \frac{R_\nu(z)\frac{dE_{\rm gw}(f_s,\theta)}{df_s}p(\theta)}{(1+z)E(z)}d\theta dz. \tag{9}$$

Finally, the spectral energy $E_{\rm gw}$ emitted by any astrophysical source can be related to the amplitudes of the plus (+) and cross (×) GW polarizations $\tilde{h}_+$ and $\tilde{h}_\times$ via [42]

$$\frac{dE_{\rm gw}}{df_s} = \frac{2\pi^2c^3d_L^2f^2}{G(1+z)^2}\left\langle|\tilde{h}_+(f,\theta)|^2+|\tilde{h}_\times(f,\theta)|^2\right\rangle_{\Omega_s}, \tag{10}$$

where the right-hand side is averaged over the source orientations Ω_s.

IV. THE CBC POPULATION MODELS

In the previous sections, we provided the motivation and the methods to calculate $\Omega_{\rm cbc,\,unres}$, the unresolved SGWB from CBCs. Now we describe the models we use for the astrophysical population of CBCs, focusing in particular on detectability by XG GW detectors. Several studies have shown that almost all of the BBHs will be individually resolvable by these detectors [14,15,26] and that the unresolvable background from BBHs will be several orders of magnitude smaller than the corresponding background from BNS. Therefore, we assume that the unresolvable SGWB arising from the BBH population is negligible and limit ourselves to the NSBH and BNS populations.

Since XG detectors will likely be able to detect all compact binaries that merge at low redshifts, such events will not contribute to the unresolved CBC SGWB. On the other hand, mergers at high redshifts will often not be individually resolvable, making them important contributors to the unresolved CBC SGWB. Therefore, we incorporate realistic star-formation-based redshift distribution models paired with a model of merger delay-time distributions. This is described further in Sec. IV A.

For all considered astrophysical populations, we assume that tidal effects and any eccentricity effects are negligible as they will be subdominant. The GW signal of such binaries can then be described by a set of 15 source parameters θ, of which eight are intrinsic and seven are extrinsic. Intrinsic parameters include the component masses m_1 and m_2 and the three-dimensional spin vectors

TABLE I. Different populations of the various source parameters used in calculating the SGWB from CBCs. See Sec. IV for further details.

	Model				
Parameter	PDB-PL	NSBH-PL	NSBH-G	BNS-G	BNS-PL
$\mathcal{R}_0(\Lambda_{\rm GW})$	Rate-inclusive	Rate-inclusive	Rate-inclusive	Drawn from PDB-IND analysis [8,44–46]	Drawn from PDB-IND analysis [8,44–46]
m_1	PDB with power-law pairing [8,44,45]	Power law [47]	Power law [47]	Double Gaussian [48]	Power law [8,44,49]
m_2	PDB with power-law pairing [8,44,45]	Power law pairing [47]	Gaussian pairing [47]	Uniform [48]	Random pairing [8,44,49]
z	Madau-Fragos SFR [50] (fiducial) Long gamma-ray burst SFR [51]				
$t_d^{\rm min}$	20 Myr				
$\vec{\chi}_1, \vec{\chi}_2$	0				
$\cos\iota$, $\cos\delta$	Uniform in $[-1, 1]$				
α, ψ, ϕ_c	Uniform in $[0, 2\pi]$				

$\vec{\chi}_1$ and $\vec{\chi}_2$. Since spins are expected to have a subdominant effect on the SGWB, we also set them to zero [26,43]. Extrinsic parameters include the redshift z, the right ascension and declination (α, δ), the polarization angle ψ, the inclination angle ι, the coalescence phase ϕ_c, and the coalescence time t_c.[5] We draw $\cos\iota$, $\cos\delta$, α, ψ, and ϕ_c from uniform distributions.

The rate and mass models are described in the following subsections, and the full distributions are summarized in Table I.

A. The redshift distributions

Compact binaries experience a delay time t_d between their formation at z_f and merger at z, where z_f is the zero-age main-sequence "formation" redshift. We calculate the delay time as the difference between the cosmological lookback time [52] at z_f and z,

$$t_d = t_L(z_f) - t_L(z). \tag{11}$$

We assume a delay time distribution of $p(t_d) \propto t_d^{-1}$ as suggested by stellar evolution and population synthesis models [53,54]. The GW and Galactic pulsar observations [55,56] are also consistent with such a distribution, although Galactic populations likely harbor an excess of sources that will merge rapidly. An analysis using localized short gamma-ray bursts potentially finds steeper time-delay distributions, but it does not include selection effects [57]. We set the maximum delay time $t_d^{\rm max}$ to the Hubble time to limit ourselves to binaries that will merge in the age of the Universe. We set a fiducial minimum delay time $t_d^{\rm min}$ of 20 Myr, which is approximately how long massive binaries take to evolve into two neutron stars [58–60]. It is also consistent with observations of binary pulsar merger times and of short gamma-ray bursts in both late- and early-type galaxies [58,61].

We convolve t_d with a star formation rate (SFR) model $R_f(z_f)$ to calculate the source-frame CBC merger rate density per comoving volume [55]

$$R_m(z) \propto \int_{t_d^{\rm min}}^{t_d^{\rm max}} R_f(\tilde{z}[t_L(z) + t_d]) p(t_d) dt_d, \tag{12}$$

where $\tilde{z}$ is the formation redshift. We normalize Eq. (12) as

$$R_{\nu,cbc}(z) = \frac{\mathcal{R}_0}{R_m(z=0)} R_m(z), \tag{13}$$

such that $R_{\nu,cbc}(z=0) = \mathcal{R}_0$ is the inferred local source-frame CBC merger rate density per comoving volume obtained from population analysis (see Sec. IV B) for CBCs of type ν. Using Eq. (7), we calculate the observed differential CBC merger rate,

$$\frac{dR_{o,cbc}(z)}{dz} = R_{\nu,cbc}(z) \frac{1}{1+z} \frac{dV_c}{dz}(z). \tag{14}$$

We simulate CBCs up to redshift $z = 10$ as we expect minimal star formation beyond this redshift and therefore no CBCs [62]. Our fiducial SFR model is the Madau-Fragos SFR [50],

$$R_f(z_f) \propto \frac{(1+z_f)^{2.6}}{1 + \left(\frac{1+z_f}{3.2}\right)^{6.2}}. \tag{15}$$

[5]The choice of t_c does not affect the calculation of $\Omega_{\rm cbc,\,unres}$, since it depends only on the GW power.

B. The mass distributions and rates

We now describe the mass distributions and local merger rate densities $\mathcal{R}_0$ we use to simulate the CBC population. We consider several population models, fit to LVK data up until the end of the third observing run via Bayesian inference. We also consider models of mass distribution fit to Galactic double neutron stars. Considering several models enables us to characterize systematic astrophysical modeling uncertainties that could come from using strongly parametrized models. Each model has a statistical uncertainty on the population that we marginalize over. Additionally in each model, a single set of hyperparameters $\Lambda_{\rm GW}$ characterizes a single CBC population. We assume that only the overall rate, not the mass distribution, evolves with redshift according to Eq. (12).

For each model, we self-consistently include the rates inferred by it when available [63]. We refer to such models as "rate-inclusive" models. For models where such information is not available—which we refer to as "rate-marginalized" models—we randomly pair each hyperparameter sample with a $\mathcal{R}_0$ posterior from an LVK O3b population model [44] that estimates rates. For clarity, we rewrite Eq. (14) for cases where $\mathcal{R}_0$ depends on $\Lambda_{\rm GW}$ [i.e., $\mathcal{R}_0(\Lambda_{\rm GW})$] as

$$\frac{dR_{o,cbc}(z,\Lambda_{\rm GW})}{dz} = R_{v,cbc}(z,\Lambda_{\rm GW})\frac{1}{1+z}\frac{dV_c}{dz}(z). \quad (16)$$

The various mass-rate model configurations are described below and summarized in Table I.

1. Neutron-star black-hole models

We model the NSBH mass distribution using the Bayesian population analyses from Ref. [47]. We assume that the distribution of the primary mass m_1 follows the truncated power law [64]

$$\pi(m_1|\gamma, m_{1,\rm min}, m_{1,\rm max}) \propto \begin{cases} m_1^{-\gamma}, & \text{if } m_{1,\rm min} \le m_1 \le m_{1,\rm max} \\ 0, & \text{otherwise} \end{cases}, \quad (17)$$

with a power-law index γ, minimum m_1 cutoff $m_{1,\rm min}$, and maximum m_1 cutoff $m_{1,\rm max}$.

We consider two pairing functions to get the distribution of the secondary mass. The first is a power-law pairing function [65], which we refer to as the NSBH-PL model:

$$\pi(q|\beta, m_1, m_{2,\rm max}) \propto \begin{cases} q^{\beta}, & \text{if } q_{\rm min}(m_1) \le q \le q_{\rm max}(m_1, m_{2,\rm max})) \\ 0, & \text{otherwise} \end{cases}, \quad (18)$$

where $q = m_2/m_1$ is the mass ratio and β is a power-law index. The second is a truncated-Gaussian pairing function [47], which we refer to as the NSBH-G model:

$$\pi(q|\mu, \sigma, m_1, m_{2,\rm max}) \propto \begin{cases} \mathcal{N}(q|\mu,\sigma), & \text{if } q_{\rm min}(m_1) \le q \le q_{\rm max}(m_1, m_{2,\rm max})) \\ 0, & \text{otherwise} \end{cases}, \quad (19)$$

where $\mathcal{N}(q|\mu,\sigma)$ is a Gaussian with mean μ and standard deviation σ. For both models, we set the minimum neutron star (NS) mass $m_{2,\rm min} = 1M_\odot$ so that the minimum mass ratio cutoff $q_{\rm min} = 1/m_1$. The maximum mass ratio cutoff is set as $q_{\rm max} = \min(m_{2,\rm max}/m_1, 1)$, where the maximum NS mass $m_{2,\rm max}$ is a free parameter drawn uniformly between $1.97M_\odot$ and $2.7M_\odot$. While the ranges of m_1 and m_2 differ based on the particular hyperparameter values, the broadest possible range is $m_1 \in [2, 20]M_\odot$ and $m_2 \in [1, 2.7]M_\odot$. We refer the reader to Ref. [47] for a more detailed overview of the models.

Both the NSBH-PL and NSBH-G models are rate-inclusive models that self-consistently calculate $\mathcal{R}_0$. Hence, for each hyperparameter sample in both analyses, we set $\mathcal{R}_0$ to the associated posterior $\mathcal{R}_0(\Lambda_{\rm GW})$.

2. Power law + dip + break model

We next consider the Power law + dip + break (PDB) model used in the LVK GWTC-3 analysis [8,44–46]. This model fits the entire mass spectrum of CBCs eschewing the difference between black holes and neutron stars. The PDB model fits both the primary and secondary masses using a common distribution $\pi_{\rm pdb}(m|\vec{\Lambda})$ that is based on a broken-power law and includes a "notch filter" to model a potential mass gap between 3 and $5M_\odot$. We refer the reader to Ref. [45] for a detailed overview of the model.

We then use a power-law pairing function to pair the primary and secondary masses [44,65]:

$$g(m_1, m_2, \beta) = \begin{cases} q^{\beta}, & \text{if } m_2 \le m_1 \\ 0 & \text{otherwise} \end{cases}. \quad (20)$$

This gives the following joint mass distribution, which we refer to as the PDB-PL model:

$$\pi_{\text{PDB-PL}}(m_1, m_2|\vec{\Lambda}, \beta) \propto \pi_{\rm pdb}(m_1|\vec{\Lambda})\pi_{\rm pdb}(m_2|\vec{\Lambda}) \times g(m_1, m_2, \beta). \quad (21)$$

While PDB-PL is a rate-inclusive model, we need to account for the fact that the model natively incorporates BBH mergers as well. In order to calculate rates that only include the NSBH and BNS parts of the spectrum, we correct the rates by the fraction of NSBH and BNS mergers that this model predicts (at each point in the hyperparameter space). Since we need systems to have at least one neutron star, we limit m_2 to span $[1, 3]M_\odot$ while allowing m_1 to span $[1, 100]M_\odot$ as defined in the original model [44].

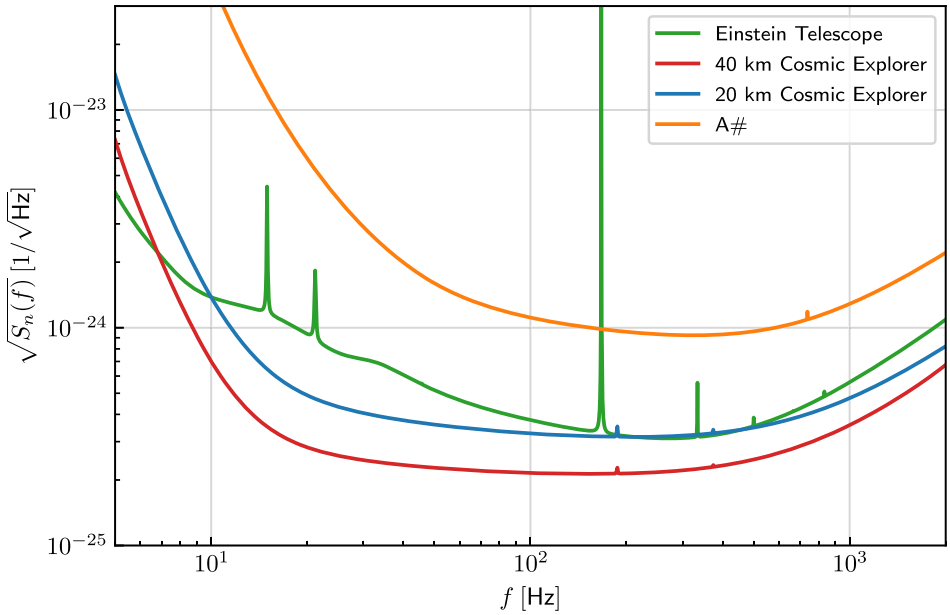

FIG. 1. Amplitude spectral densities $\sqrt{S_n}$ for the detectors in our networks. Note that the ET curve corresponds to the sensitivity of a single interferometer in the ET triangular configuration.

3. Binary neutron star models

We model the BNS mass distribution using two different rate-marginalized models. The first model is motivated through observations of Galactic double neutron stars, which provide the largest and most well-constrained sample of such systems. This model, which we refer to as BNS-G, is based on the most favored model from the population analysis of the 17 observed Galactic BNSs by Ref. [48]. In particular, the primary neutron-star mass follows a double-Gaussian mixture model,

$$\pi(m_1|\gamma,\mu_1,\sigma_1,\mu_2,\sigma_2) = \frac{\gamma}{\sigma_1\sqrt{2\pi}}e^{-\frac{(m_1-\mu_1)^2}{2\sigma_1}} + \frac{1-\gamma}{\sigma_2\sqrt{2\pi}}e^{-\frac{(m_2-\mu_2)^2}{2\sigma_2}}, \quad (22)$$

where γ $(1-\gamma)$, μ_1 (μ_2), and σ_1 (σ_2) give the weight, mean, and standard deviation of the first (second) peak, respectively. The secondary neutron-star mass is drawn uniformly within the range

$$\pi(m_2|m_{2,\min},m_{2,\max}) = U[m_{2,\min},m_{2,\max}], \quad (23)$$

with minimum and maximum cutoff $m_{2,\min}$ and $m_{2,\max}$, respectively. As usual, we assume that $m_2 \leq m_1$. We note that both the double-Gaussian and uniform distributions are truncated at $0.8M_\odot$ and $2M_\odot$ to reflect the prior ranges of the analysis from Ref. [48].

While the analysis in Ref. [48] relies on observations of only Galactic BNSs, we assume in our usage of the BNS-G model that it is extendable to all redshifts and metallicities. Note, however, that the BNS mass distribution inferred with Galactic observations is potentially inconsistent with GW observations. This is especially highlighted by the BNS merger GW190425 [66], which has a total mass heavier than that of typical Galactic double neutron stars and could potentially have formed through different formation channels [67].

Hence, we include a second model, which we call BNS-PL, based on the BNS POWER mass distribution inferred from all the neutron star systems detected through GWs [8,44,49]. In the BNS-PL model, both the primary and secondary masses are paired randomly after each has been drawn from a power-law distribution

$$\pi(m|\gamma,m_{\min},m_{\max}) \propto m^\gamma, \quad (24)$$

with a power-law index γ and minimum (maximum) mass cutoff $m_{\min}$ ($m_{\max}$). While the neutron star POWER model is used in Ref. [44] to infer the mass distribution from both BNSs and NSBHs, we only consider the BNS case here.

Since our BNS models are all rate marginalized, we model their rate distributions by drawing $\mathcal{R}_0$ posteriors from the rate-inclusive PDB random-pairing model (which we refer to as PDB-IND) [44,45] fit to LVK GWTC-3 data. Similar to Sec. IV B 2, we correct the rates inferred by PDB-IND to include only the fraction of systems that are BNSs. This means restricting the masses to $m_1, m_2 \in [1,3]M_\odot$ for the BNS-PL model, but to $m_1, m_2 \in [1,2]M_\odot$ for the BNS-G model to be consistent with the mass ranges from Refs. [44,48].

V. DETECTOR NETWORKS

We consider four different possible networks of XG detectors, using the latest detector designs described in Refs. [15,16]. Using the GW simulation package GWBENCH [68], we consider the `CE-40` and `CE-20` options for the proposed 40-km arm and 20-km arm CE sensitivities respectively [15,16], the `A#` option for the proposed 4-km arm A# sensitivity [69], and the `ET-10-XYL` option for the proposed triangular "xylophone" 10-km arm ET sensitivity [70]. Figure 1 shows the amplitude spectral density $\sqrt{S_n(f)}$ of each detector considered.

Since an SGWB is detected by cross-correlating data observed separately by at least two detectors, we consider only multiple-detector networks [71]. We consider the `CE-A` (coast of Washington, USA), `CE-B` (coast of Texas, USA), `ETS` (slightly South of Virgo's current location at Cascina, Italy), and `LLO` (current location of the LIGO-Livingston Observatory at Livingston, Louisiana, USA) facility locations specified in Table II of Ref. [16], which we point to for the details.

We consider four different networks of detectors:

(1) A *fiducial* three-detector network including one `CE-40` at `CE-A`, one `CE-20` at `CE-B`, and one `ET-10-XYL` at `ETS`.
(2) An *alternate* three-detector network including one `CE-40` at `CE-A`, one `ET-10-XYL` at `ETS`, and one `A#`-upgraded detector at `LLO`.
(3) An *alternate* two-detector network including one `CE-40` at `CE-A`, and one `CE-20` at `CE-B`.
(4) An *alternate* two-detector network including one `CE-40` at `CE-A`, and one `ET-10-XYL` at `ETS`.

We choose the same three-detector networks as those proposed in Refs. [15,16] to make it easy to compare with existing and future literature. While the future development of ET has been officially confirmed, we specifically explore a two-detector network configuration that does not include ET in order to evaluate the usefulness of and aid in the detector design of CE facilities in detecting astrophysically and cosmologically arising SGWBs even in the absence of ET.

Throughout the paper, we set a minimum frequency of 5 Hz as a conservative choice based on estimates of Newtonian noise [23]. In addition, we set a maximum frequency of 2000 Hz. For each network, we use the same 3σ power-law integrated (PI) curves [26,72] as Ref. [16][6] in order to measure the ability of the network to detect SGWB signals. We refer the reader to Ref. [16] for the overlap reduction functions [26,72] of the various detector pairs comprising the networks described in this section.

[6]Obtained through private communication with the authors.

VI. SIMULATING THE SGWB: A MONTE CARLO APPROACH

In the previous sections, we have described the population models and the detector networks that we use. In this section, we describe the simulation and the calculation of the unresolved SGWB using Eq. (9) and Eq. (10) for which we adopt a Monte Carlo approach [18,31,58,73,74]. We use the GWBENCH simulation platform [68] to generate GW waveforms for nonspinning quasicircular binaries neglecting tidal effects. GWBENCH naturally accounts for the Earth's rotation and its impact on the antenna patterns which is important since BNSs can last for several hours in the observing band of XG detectors [68]. We use IMRPhenomD [75,76] as our waveform approximant.[7]

For each population configuration described in Sec. IV and summarized in Table I, we are interested in calculating $\Omega_{\rm cbc,\,unres}$. To account for astrophysical uncertainties, we draw 2000 hyperparameter samples from the inferred population distributions and estimate $\Omega_{\rm cbc,\,unres}$ for each sample.

To do this in a computationally tractable way, we first simulate 10^5 waveforms each for NSBHs and BNSs drawn from broad fiducial population distributions.[8] We then apply rejection sampling to draw a population corresponding to any particular hyperparameter draw. We estimate the mean number of sources needed for a CBC model ν with a set of hyperparameters $\Lambda_{\rm GW}$ and observation time T as

$$\langle N_\nu(\Lambda_{\rm GW})\rangle = \int_0^{z_{\rm max}} R_\nu(z,\Lambda_{\rm GW})\frac{dV_c}{dz}\frac{dz}{1+z}T, \tag{25}$$

and draw the actual number of sources through a Poisson draw,

$$N_\nu(\Lambda_{\rm GW}) \sim \texttt{Poiss}(\lambda = \langle N_\nu(\Lambda_{\rm GW})\rangle). \tag{26}$$

In order to estimate $\Omega_{\rm cbc,\,unres}$, we first need to extract only the unresolvable signals from this population. To do this, we first compute the matched-filter signal-to-noise ratio (SNR) $\rho_j^{\rm mf}$ of the signal, defined for detector j with noise power spectral density $S_{n,j}(f)$ as [77]:

$$\rho_j^{\rm mf} = \left[4\int_0^\infty \frac{|\tilde{h}_j(f)|^2}{S_{n,j}(f)}df\right]^{1/2}. \tag{27}$$

This is, however, the optimal matched-filter SNR; in order to account for the measurement uncertainty due to detector noise, we correct the SNR as [62,78,79]

[7]Note that the choice of waveform approximant is expected to be subdominant in calculating the SGWB [26].

[8]In this fiducial population, for NSBHs we uniformly draw $m_1 \sim [2,50]$ and $m_2 \sim [1,3]$ and for BNSs we uniformly draw both $m_1, m_2 \sim [0.5,3]$.

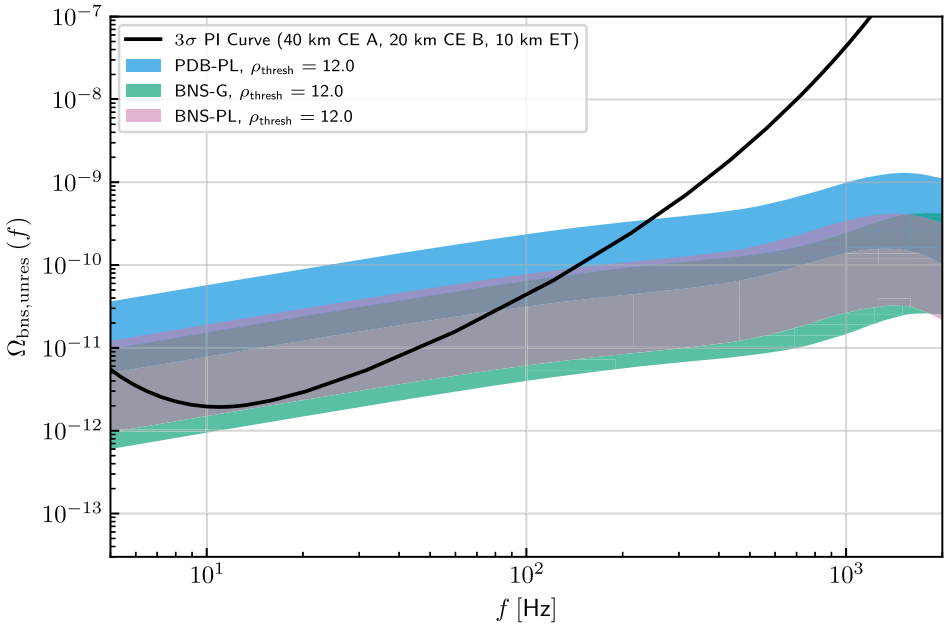

(a) $\Omega_{\mathrm{cbc,\ unres}}$ estimates for the various BNS models in Tab. I. The bands show the central 90% credible levels.

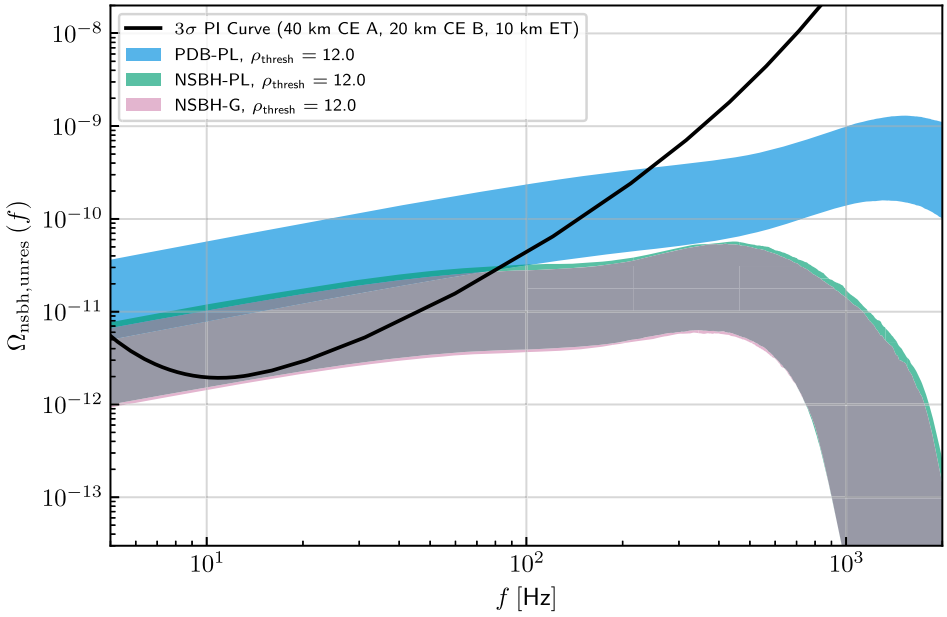

(b) $\Omega_{\mathrm{cbc,\ unres}}$ estimates for the various NSBH models in Tab. I. The bands show the central 90% credible levels.

FIG. 2. This plot shows the $\Omega_{\mathrm{cbc,\,unres}}$ estimate for the various BNS (a) and NSBH (b) models for the fiducial three-detector network described in Sec. V. The blue band in both plots is the PDB-PL model that simultaneously incorporates both the NSBH and BNS systems. Also overlaid is the 3σ PI curve that shows that the unresolved CBC backgrounds will likely be very loud.

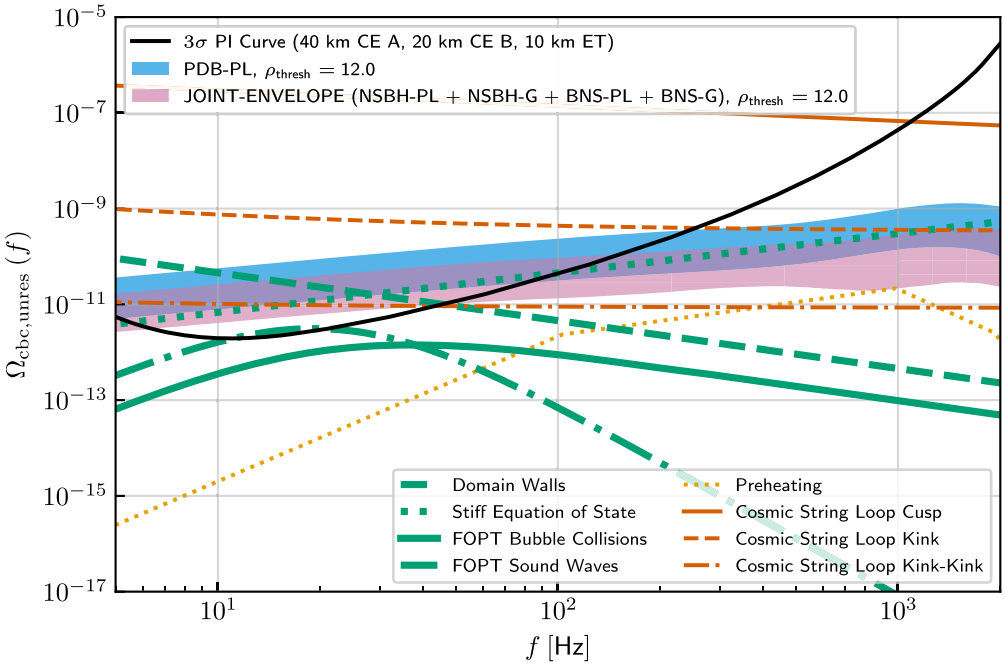

FIG. 3. A comparison of various cosmological SGWB models along with $\Omega_{\text{cbc, unres}}$ estimates for the fiducial network described in Sec. V. The blue band shows the PDB-PL model while the pink band shows the JOINT-ENVELOPE constructed from the various BNS-only and NSBH-only models in Table I. Both bands represent 90% credible intervals. The solid black curve is the 3σ PI curve.

$$\rho_j^{\text{obs}} = \rho_j^{\text{mf}} + \mathcal{N}(0,1). \tag{28}$$

We then define the optimal network SNR $\rho_{\text{net}}^{\text{obs}}$ for a network of D detectors by summing the individual observed SNRs in quadrature[9] as

$$\rho_{\text{net}}^{\text{obs}} = \sqrt{\sum_{j=1}^{D} (\rho_j^{\text{obs}})^2}. \tag{29}$$

A signal is then labeled as resolved if $\rho_{\text{net}}^{\text{obs}}$ is greater than some frequency-independent threshold ρ_{thresh}.

Once we have a population $N_\nu^{\text{unres}}(\Lambda_{\text{GW}})$ of unresolvable sources with respect to ρ_{thresh}, we calculate the GW energy flux [Eq. (6)] using a Monte Carlo sum over our simulated population [18,26,74]:

$$F_\nu(f;\Lambda_{\text{GW}}) \approx \frac{\pi c^3 f^2}{2GT} \sum_{i=1}^{N_\nu^{\text{unres}}(\Lambda_{\text{GW}})} \left[|\tilde{h}_+^i(f,\theta^i)|^2 + |\tilde{h}_\times^i(f,\theta^i)|^2 \right]. \tag{30}$$

[9]In the case of ET, ρ_j^{mf} is first calculated for each interferometer in the triangular configuration. The three ρ_j^{mf} calculations are then summed in quadrature to produce a single ρ_j^{mf} calculation for the overall triangular configuration (now considered a single detector j), prior to invoking Eq. (28).

VII. COSMOLOGICAL SGWB MODELS

To gauge the impact of the $\Omega_{\text{cbc, unres}}$, we consider several models of early Universe cosmological SGWBs that could be accessible with XG detectors in principle. These models include SGWBs from domain walls [80], first-order phase transition (FOPT) sound waves [81,82], FOPT bubble collisions [81], stiff equation of state [83], and preheating [16,84]. We also use the model spectrum for Nambu-Goto oscillating cosmic string loops (the MODEL C1 from Ref. [85]).

We note that XG detectors will not be sensitive to standard slow-roll inflation, for which $\Omega_{\text{GW}} \sim 10^{-15} - 10^{-17}$ depending on the model [9,27]. In general, these various SGWBs are highly sensitive to the choice of model parameters, but in our plots, we chose illustrative curves for Ω_{cosmo}.

VIII. RESULTS

As described in Sec. VI, for each population model in Table I, we have 2000 different draws for the unresolved CBC SGWB. These draws incorporate both the uncertainty in the rate of mergers and the astrophysical uncertainty from the population model. In Fig. 2, we show the 90% credible bands for the unresolved SGWB for the various BNS-only and NSBH-only population models, for the fiducial three-detector network from Sec. V using a fiducial threshold SNR of 12. We overlay them on top of the 3σ PI curve for this network. We assume an observation

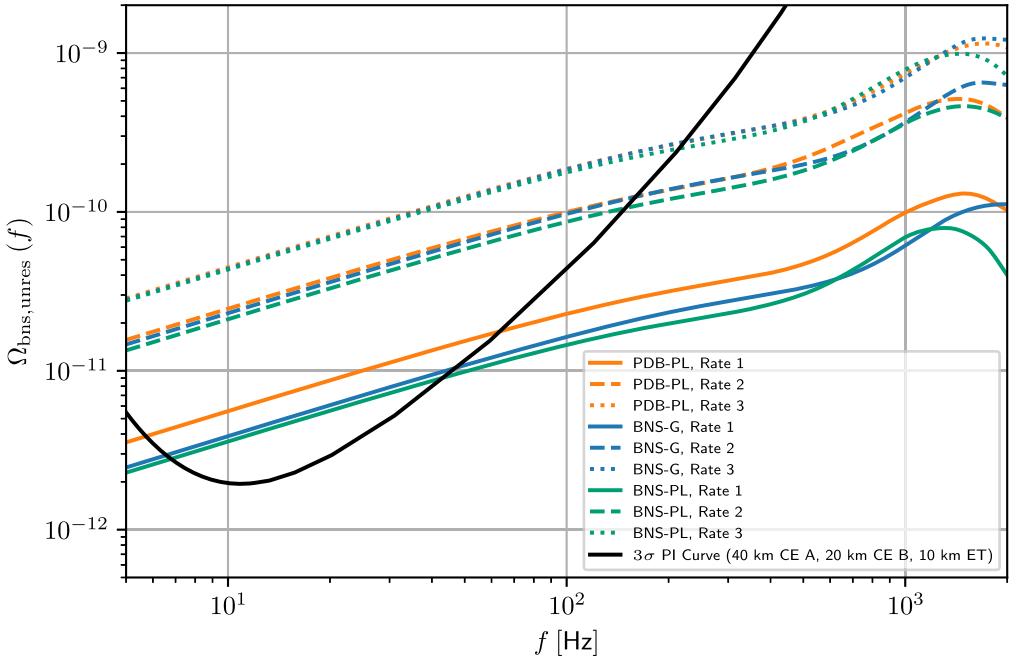

FIG. 4. The SGWB for different BNS models evaluated at three different rates using a threshold SNR of 12. We use the following NS-system rates (corrected BNS rates for BNS-PL and BNS-G): Rate 1 = 45.5(32.2) $\mathrm{Gpc^{-3}\,Yr^{-1}}$, Rate 2 = 209.3(186.6) $\mathrm{Gpc^{-3}\,Yr^{-1}}$, Rate 3 = 377.0(362.6) $\mathrm{Gpc^{-3}\,Yr^{-1}}$. While there is significant difference between the curves for various rates, the differences between the models is minimal.

time of $T = 1$ year throughout the paper. The purple band in both plots is from the PDB-PL model and is therefore higher than either of the BNS-only and NSBH-only models.

The unresolved SGWB from CBCs is above the 3σ PI curve, implying that it will very likely be detectable by XG detectors with one year of observing. In general, the width of each band in Fig. 2—which represents the total uncertainty in our estimate of the unresolved SGWB for that model—spans about 1 order of magnitude, and the bands fall out of detectability at ∼80 Hz even with XG detectors. The combined PDB-PL background, however, might be significantly detectable up to ∼200 Hz. Nevertheless, it would seem that we will only observe the SGWB due to the inspiral phase of the mergers. Similarly, while the simulations show a clear turnover for the NSBH SGWB—the morphology of which probably depends on the waveform used—it clearly happens at high frequencies, and XG detectors will probably not be able to probe this.

In addition to the PDB-PL model which naturally incorporates both BNS and NBSH mergers, we create a maximum-uncertainty envelope, which we refer to as the JOINT ENVELOPE as a means of accounting for astrophysical model systematics. This is generated by combining the BNS-only and NSBH-only models (i.e., NSBH-PL, NSBH-G, BNS-PL, BNS-G) in Table I in all possible combinations and choosing the widest band at each frequency bin.

Figure 3 shows the 90% credible band of the JOINT ENVELOPE along with the PDB-PL estimate of $\Omega_{\mathrm{cbc,\,unres}}$ for our fiducial three-detector network. We contrast these bands with several cosmological SGWB models, demonstrating that the unresolved background will likely be a major source of noise for accessing the said cosmological signals. Since the effective CBC background is the sum of unresolved and resolved components [see Eq. (3)], it also depends on the efficacy of subtraction of resolved signals. Since the subtraction residue could contribute significantly to the effective CBC background (see, e.g., [28,29]), the unresolved background we show in Fig. 3 therefore represents the floor of the noise from CBC sources. Either way, a joint simultaneous analysis of the CBC background and the cosmological background will be necessary for the detection of the latter. We note again that the cosmological SGWB curves themselves can change depending on the choice of parameters. In the Appendix, we present similar results for the three alternate detector networks described in Sec. V.

Further exploring the uncertainty in the $\Omega_{\mathrm{cbc,\,unres}}$, we see remarkable consistency between the two NSBH-only models, and similarly between the two BNS-only models. This suggests that the uncertainty in the rate is dominant, as opposed to the astrophysical uncertainty on the mass distribution. This is further confirmed by Fig. 4, where we plot the SGWB from different BNS models for three

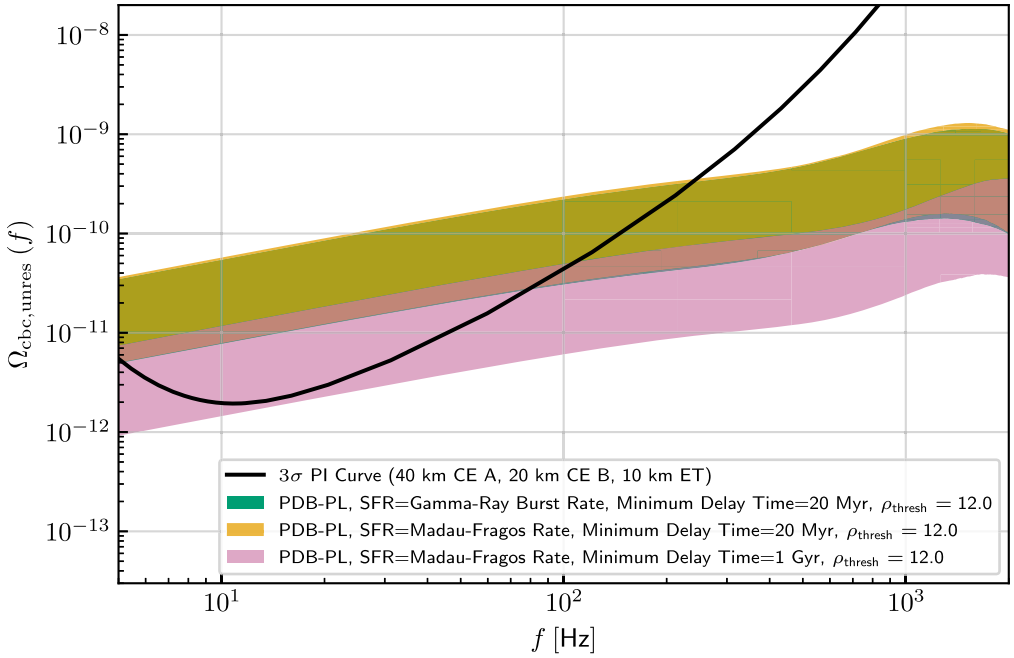

FIG. 5. 90% credible intervals of $\Omega_{\mathrm{cbc,\,unres}}$ for the PDB-PL model with three different SFR assumptions. While the green and the saffron bands are for a gamma-ray burst based SFR and the Madau-Fragos SFR respectively, the pink band is for a conservative 1 Gyr minimum time delay.

different rates. The consistency in SGWB between models at any given frequency shows that the astrophysical uncertainty is a much smaller contributor to the SGWB uncertainty than the uncertainty in the CBC rate. We find similar results for NSBHs as well. Since the number of BNSs and NSBHs observed thus far is fairly small [6–8], this means that any future detections in O4 and O5 can substantially lower the uncertainty of these bands. This is also consistent with studies such as Ref. [86], which show that the monopole of the CBC SGWB is particularly sensitive to the local merger rate.

To explore how SFR models impact our estimates of $\Omega_{\mathrm{cbc,\,unres}}$, we also used an SFR extracted from long gamma-ray burst rates following [26,51]

$$R_f(z_f) \propto \nu \frac{a e^{b(z_f - z_p)}}{a - b + b e^{a(z_f - z_p)}}, \tag{31}$$

where $\nu = 0.146 M_\odot\ \mathrm{yr}^{-1}\,\mathrm{Mpc}^3$, $z_p = 1.72$, $a = 2.80$, and $b = 2.46$. As the PDB-PL bands in Fig. 5 show, we find that the impact of the SFR model is minimal as long as the minimum delay times are small. A minimum delay time of 1 Gyr gives a significantly smaller, albeit still loud, SGWB. Note, however, that studies of Galactic systems have actually found an excess of systems with small delay times [56], meaning that the value of 1 Gyr is very conservative. We therefore conclude that the key observation of this paper, that the unresolved background will significantly impact searches for cosmological backgrounds, is likely robust to uncertainties in SFR. We have also tested our assumption of $z_{\mathrm{max}} = 10$ and find that the GW power from higher redshifts is very small.

The LVK population inference at the end of O3 tested multiple versions of the POWER model [44] including only confident events, or confident and marginal events, or confident events and GW190814.[10] While we use the last version in all our plots as the BNS-PL model, we find that the impact of this choice is negligible. In particular, our estimates of $\Omega_{\mathrm{bns,\,unres}}$ for our implemented version differ from those for the other two versions at most by 3% at 25 Hz, demonstrating that our estimates are robust with respect to this uncertainty.

Finally, we note that our fiducial threshold of $\rho_{\mathrm{thresh}} = 12$ is a conservative choice for the purposes of estimating the unresolved SGWB. An optimal threshold choice for stochastic searches maximizes resolvability and minimizes the astrophysical noise from CBCs. Our choice of ρ_{thresh} is informed by the analysis from Ref. [26], in which they search for a ρ_{thresh} that is optimal for their chosen waveform approximant (IMRPhenomD as in our study). The threshold $\rho_{\mathrm{thresh}} = 20$, in particular, was shown to be the frequency-independent optimal threshold (using IMRPhenomD) for minimizing the effective background from BNS systems, including both the subtraction residue and the unresolved background [26]. In comparison, the conservativeness of our fiducial ρ_{thresh} motivates an exploration of CBC SGWB estimates at multiple ρ_{thresh} choices.

[10] which is a population outlier [87].

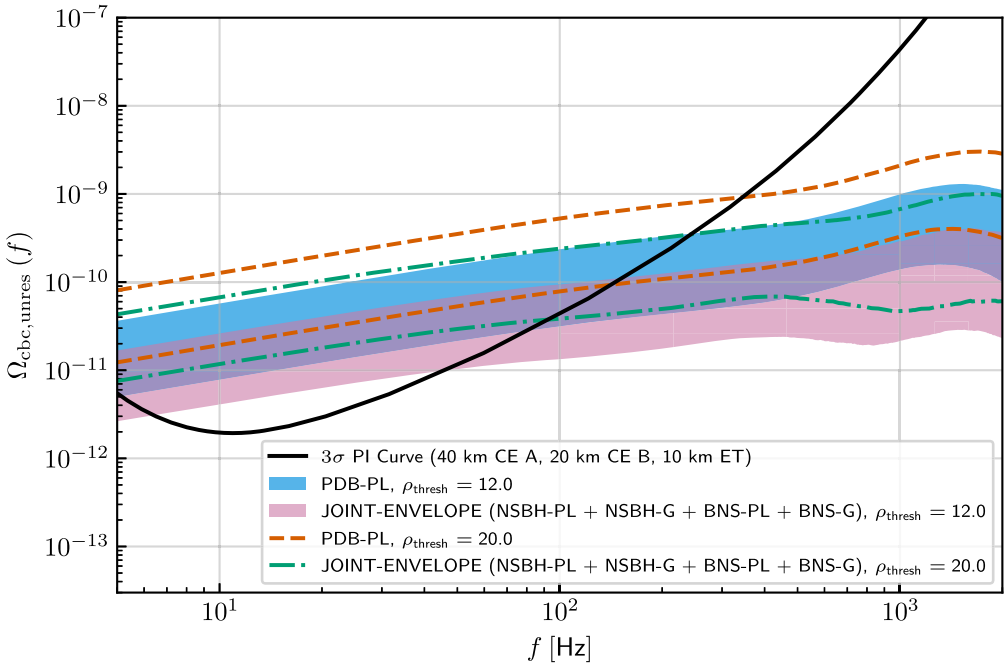

FIG. 6. 90% credible intervals of $\Omega_{\mathrm{cbc,\,unres}}$ for the PDB-PL and the JOINT-ENVELOPE models with two different ρ_{thresh} values. The filled bands show the credible intervals with $\rho_{\mathrm{thresh}} = 12$, and the dashed-dotted lines bound the intervals for $\rho_{\mathrm{thresh}} = 20$.

Figure 6 shows the PDB-PL and the JOINT-ENVELOPE bands for our fiducial ρ_{thresh} and $\rho_{\mathrm{thresh}} = 20$.

IX. IMPLICATIONS AND CONCLUSIONS

In this paper, we have presented a data-driven estimate of the strength of the unresolvable CBC background seen by XG detectors, accounting for both statistical and astrophysical systematic uncertainties. A robust implication from our study is that $\Omega_{\mathrm{cbc},d\,\mathrm{unres}}$ will be an impediment for the direct detection of many cosmological SGWB models, independent of the fidelity and efficacy of the subtraction of resolved CBC signals. Some manner of simultaneous inference of the astrophysical and cosmological background (e.g., see Refs. [88–90]) will be required at a minimum.

Given the large number of resolvable CBC signals that we expect, it is also possible that their population inference can be used as a strong prior for $\Omega_{\mathrm{cbc,\,unres}}$. While this could make inferring multiple backgrounds easier, this effort could be hindered by the efficacy of subtraction. Moreover, using the resolvable signals to form a prior could create a systematic bias because the resolvable and unresolvable sources come from different redshifts [91].

However, this also makes $\Omega_{\mathrm{cbc,\,unres}}$ astrophysically interesting in its own right by allowing us to study compact binary populations at high redshifts [62,92]. Since we will confidently detect $\Omega_{\mathrm{cbc,\,unres}}$ with XG detectors, this represents a clear science case that can inform detector design. For this purpose, in Table II we provide figures of merit of the level of $\Omega_{\mathrm{cbc,unres}}$ for various detector networks at two reference frequencies.

Our results also help inform the target efficacy of subtraction techniques for XG detectors. The optimal level of subtraction is one that leaves a residue not significantly higher than $\Omega_{\mathrm{cbc,\,unres}}$. At the same time, a subtraction technique that leaves a residue substantially lower than $\Omega_{\mathrm{cbc,\,unres}}$ will not be ideal and will likely be computationally expensive from a statistical point of view. Our figures of merit for the various networks in Table II will again be useful in informing the optimal efficacy of subtraction that algorithms should target.

Instead of subtraction, one can also infer the parameters of CBC signals without any threshold. This Bayesian "global fit" technique was first developed in Ref. [93], with various extensions studied in Refs. [94–97]. Reference [97] in particular showed how a cosmological (non-CBC) background can be incorporated into this formalism for simultaneous inference. While this statistical formalism holds much promise because it removes the need both for subtracting the resolved CBC signals and for separately inferring the unresolved CBC background, it is also computationally very expensive, which can make running it on long stretches of data untenable. Moreover, the method is susceptible to subtle systematics [95] and can struggle to deal with overlapping signals, both of which can make an application on real XG data challenging.

TABLE II. $\Omega_{\mathrm{cbc,\,unres}}$ for different networks at two reference frequencies for the PDB-PL model and the JOINT-ENVELOPE. The quoted numbers correspond to median values with 90% uncertainties. We present these estimates as figures of merit for both detector design and subtraction algorithms.

		$\log_{10}\Omega_{\mathrm{cbc,unres}}$		
Model	f	$\rho_{\mathrm{thresh}}=12$	$\rho_{\mathrm{thresh}}=20$	$\rho_{\mathrm{thresh}}=40$
40 km CE A, 20 km CE B, 10 km ET				
JOINT-ENVELOPE	25 Hz	$-10.8^{+0.4}_{-0.4}$	$-10.3^{+0.4}_{-0.4}$	$-10.0^{+0.3}_{-0.4}$
	250 Hz	$-10.3^{+0.5}_{-0.4}$	$-9.9^{+0.4}_{-0.4}$	$-9.6^{+0.4}_{-0.4}$
PDB-PL	25 Hz	$-10.4^{+0.4}_{-0.5}$	$-10.0^{+0.4}_{-0.4}$	$-9.8^{+0.4}_{-0.4}$
	250 Hz	$-9.8^{+0.4}_{-0.5}$	$-9.5^{+0.4}_{-0.5}$	$-9.3^{+0.4}_{-0.4}$
40 km CE A, 10 km ET, 4 km A# LLO				
JOINT-ENVELOPE	25 Hz	$-10.6^{+0.4}_{-0.4}$	$-10.3^{+0.4}_{-0.4}$	$-10.0^{+0.4}_{-0.4}$
	250 Hz	$-10.2^{+0.4}_{-0.4}$	$-9.8^{+0.4}_{-0.4}$	$-9.6^{+0.4}_{-0.4}$
PDB-PL	25 Hz	$-10.3^{+0.4}_{-0.5}$	$-10.0^{+0.4}_{-0.5}$	$-9.8^{+0.4}_{-0.5}$
	250 Hz	$-9.8^{+0.4}_{-0.5}$	$-9.4^{+0.4}_{-0.5}$	$-9.3^{+0.4}_{-0.5}$
40 km CE A, 20 km CE B				
JOINT-ENVELOPE	25 Hz	$-10.6^{+0.4}_{-0.4}$	$-10.2^{+0.4}_{-0.4}$	$-10.0^{+0.4}_{-0.3}$
	250 Hz	$-10.1^{+0.4}_{-0.4}$	$-9.8^{+0.4}_{-0.4}$	$-9.6^{+0.4}_{-0.3}$
PDB-PL	25 Hz	$-10.2^{+0.4}_{-0.5}$	$-9.9^{+0.4}_{-0.5}$	$-9.8^{+0.4}_{-0.4}$
	250 Hz	$-9.7^{+0.4}_{-0.5}$	$-9.4^{+0.4}_{-0.5}$	$-9.2^{+0.4}_{-0.4}$
40 km CE A, 10 km ET				
JOINT-ENVELOPE	25 Hz	$-10.6^{+0.4}_{-0.4}$	$-10.3^{+0.4}_{-0.4}$	$-10.0^{+0.4}_{-0.4}$
	250 Hz	$-10.2^{+0.4}_{-0.4}$	$-9.8^{+0.4}_{-0.4}$	$-9.6^{+0.4}_{-0.4}$
PDB-PL	25 Hz	$-10.3^{+0.4}_{-0.5}$	$-10.0^{+0.4}_{-0.5}$	$-9.8^{+0.4}_{-0.5}$
	250 Hz	$-9.8^{+0.4}_{-0.5}$	$-9.4^{+0.4}_{-0.5}$	$-9.3^{+0.4}_{-0.5}$

Finally, we discuss some of the caveats of this study. One of the most important assumptions we made is the specific form of the SFR distribution. While we have tried two different SFR models as we show in Fig. 5, uncertainties on the rate naturally increase at higher redshift. For instance, observations with the James Webb Space Telescope show heightened star formation at high redshifts, which might imply a louder CBC background, and more observation in the near future might make the picture clearer [98,99]. Another effect that is somewhat related, which we did not consider here is the effect of metallicity [100–105]. This would again predominantly impact the rate at higher redshifts.

We have assumed that nearly all BBH mergers would be resolved, and thereby contribute negligibly to $\Omega_{\mathrm{cbc,\,unres}}$. However, population synthesis studies with Population III stars suggest that the resultant BBHs could be a non-negligible source of the unresolved background with XG detectors [101,103,106,107]. Nevertheless, no population III stars have been observed so far, and large uncertainties remain on their merger rates and other properties. These will likely only be resolved after XG detectors become operational and detect binaries at high redshifts [108].

On the GW waveform side, we have assumed zero spins and tidal effects. While these are all subdominant compared to the mass distributions, it is possible that the spins in particular might have a noticeable impact on $\Omega_{\mathrm{cbc,\,unres}}$ given the lengths of the signals in XG detectors.

ACKNOWLEDGMENTS

We thank Salvatore Vitale, Emanuele Berti, Vuk Mandic, Haowen Zhong, and Vishal Baibhav for helpful discussions. We thank Amanda Farah and Philippe Landry for their help with the LVK population analyses and Sylvia Biscoveanu for her help with the NSBH population analyses and for providing PI curves for XG detectors. D. S. B. is supported by the National Science Foundation (NSF) Graduate Research Fellowship Program under Grant No. DGE-2234667. Any opinion, findings, and

conclusions or recommendations expressed in this material are those of the authors and do not necessarily reflect the views of the NSF. D. S. B. was supported by a CIERA Post-Baccalaureate Research Fellowship during the majority of this research. D. S. B. acknowledges partial support for this project from NASA through a NASA Illinois Space Grant. S. B. acknowledges support from the NSF Grant No. PHY-2207945. Z. D. is supported by the CIERA Board of Visitors Research Professorship. V. K. is partially supported through a CIFAR Senior Fellowship, a Guggenheim Fellowship, the Gordon and Betty Moore Foundation (Grant Award No. GBMF8477), and from Northwestern University, including the Daniel I. Linzer Distinguished University Professorship fund. This material is based upon work supported by NSF's LIGO Laboratory which is a major facility fully funded by the National Science Foundation. This research has made use of data obtained from the Gravitational Wave Open Science Center (gwosc.org), a service of LIGO Laboratory, the LIGO Scientific Collaboration, the Virgo Collaboration, and KAGRA. LIGO Laboratory and Advanced LIGO are funded by the United States NSF as well as the STFC of the United Kingdom, the Max-Planck-Society (MPS), and the State of Niedersachsen/Germany for support of the construction of Advanced LIGO and construction and operation of the GEO 600 detector. Additional support for Advanced LIGO was provided by the Australian Research Council. Virgo is funded, through the European Gravitational Observatory (EGO), by the French Centre National de Recherche Scientifique (CNRS), the Italian Istituto Nazionale di Fisica Nucleare (INFN), and the Dutch Nikhef, with contributions by institutions from Belgium, Germany, Greece, Hungary, Ireland, Japan, Monaco, Poland, Portugal, and Spain. K. A. G. R. A. is supported by the Ministry of Education, Culture, Sports, Science and Technology (MEXT), Japan Society for the Promotion of Science (JSPS) in Japan; National Research Foundation (NRF) and Ministry of Science and ICT (MSIT) in Korea; Academia Sinica (AS) and National Science and Technology Council (NSTC) in Taiwan. The authors are grateful for computational resources provided by the LIGO Laboratory and supported by NSF Grants No. PHY-0757058 and No. PHY-0823459. Lastly, we acknowledge the efforts of the CE Consortium and ET Collaboration in the planning and development of XG GW detectors. This manuscript carries an LSC DCC number LIGO-P2300334.

APPENDIX: STOCHASTIC BACKGROUNDS FROM ALTERNATE DETECTOR NETWORKS

In this Appendix, we show the results for the alternate detector networks that we consider in this study. Figure 7 shows our $\Omega_{\mathrm{cbc,\,unres}}$ estimates for the PDB-PL and JOINT-ENVELOPE models for the various alternate detector networks we consider in Sec. V. Also overlaid are the different cosmological models discussed in Sec. VII. The equivalent plot for our fiducial network is Fig. 3. Finally, Fig. 8 overlays the PDB-PL model $\Omega_{\mathrm{cbc,\,unres}}$ estimates for all our considered networks as a means of direct comparison.

From Fig. 8, we find that the level of $\Omega_{\mathrm{cbc,\,unres}}$ is much more significantly impacted by the uncertainties in the CBC population than by the sensitivity changes arising from choosing different network configurations. Hence, at our current level of understanding of the CBC population, it would be difficult to determine which network configuration will see a lower $\Omega_{\mathrm{cbc,\,unres}}$. However, we find that the addition of a 4-km $A^{\#}$ detector to a network of 1 ET and 1 40-km CE produces an almost negligible effect on the level of the unresolved CBC background, potentially making the addition of an $A^{\#}$ detector to a XG network unhelpful in reducing $\Omega_{\mathrm{cbc,\,unres}}$.

With a larger observed CBC population perhaps by the end of O5, we might be able to make a more robust statement about which of these XG detector configurations will see a quieter unresolved CBC background. Therefore, we leave a more exhaustive study comparing the level of the unresolved CBC background resulting from different detector networks to future work.

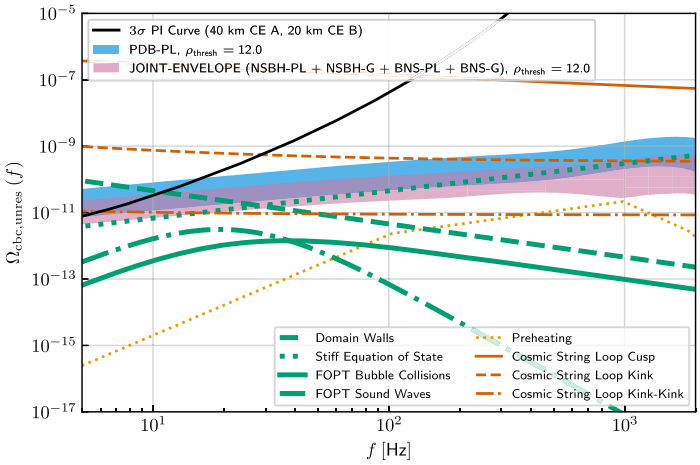

(a) $\Omega_{\mathrm{cbc,\ unres}}$ estimates for a network consisting of a 40-km CE A and a 20-km CE B.

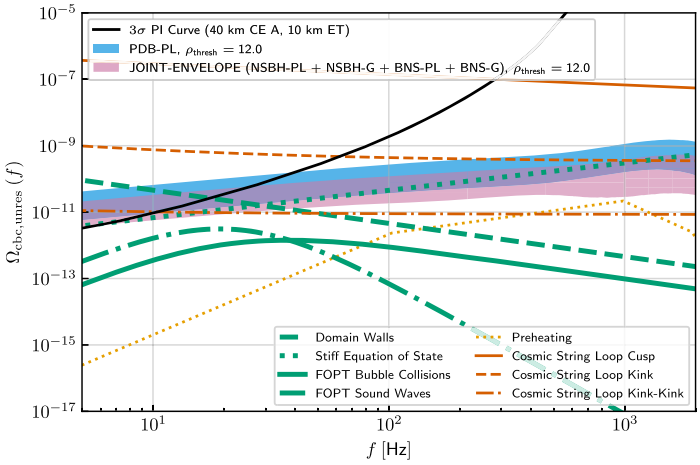

(b) $\Omega_{\mathrm{cbc,\ unres}}$ estimates for a network consisting of a 40-km CE A and an ET.

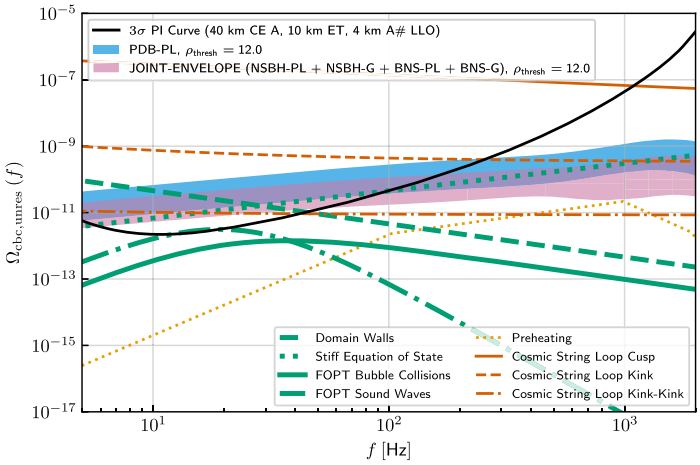

(c) $\Omega_{\mathrm{cbc,\ unres}}$ estimates for a network consisting of a 40-km CE A, an A$^{\#}$ at LLO, and an ET.

FIG. 7. A comparison of various cosmological SGWB models along with $\Omega_{\mathrm{cbc,\ unres}}$ estimates for the various alternate detector networks (a), (b), and (c) we consider in Sec. V. The blue band shows the PDB-PL model while the pink band shows the JOINT-ENVELOPE constructed from the various BNS-only and NSBH-only models in Table I. Both bands represent 90% credible intervals. The solid black curve is the 3σ PI curve.

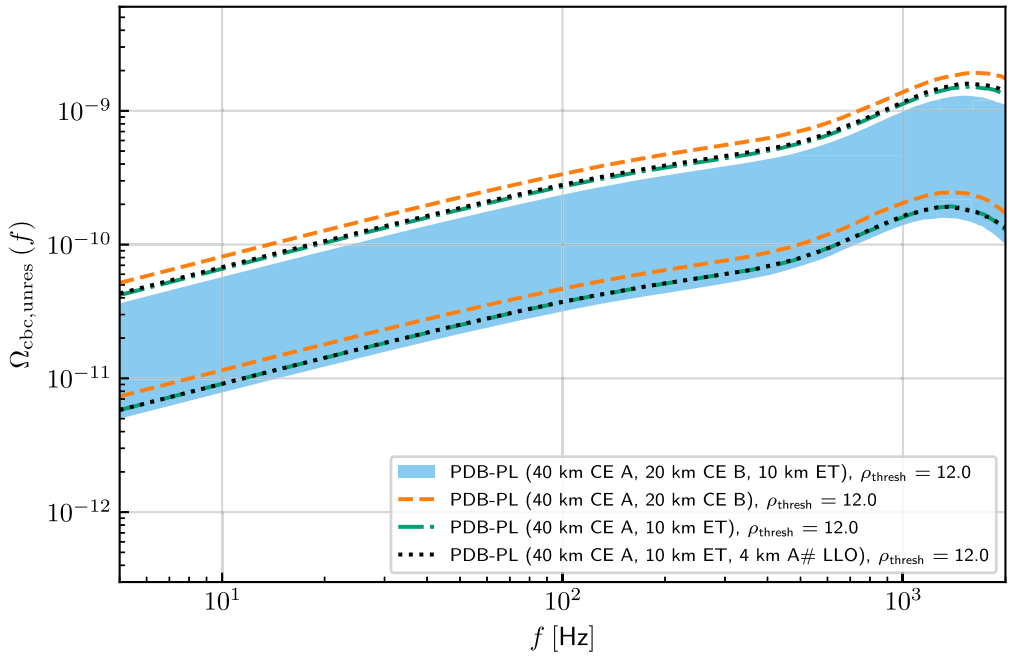

FIG. 8. A comparision of the 90% credible intervals of $\Omega_{\mathrm{cbc,unres}}$ for the PDB-PL model for the four different detector networks defined in Sec. V.

[1] J. Aasi *et al.* (LIGO Scientific Collaboration), Advanced LIGO, Classical Quantum Gravity **32**, 074001 (2015).

[2] B. P. Abbott *et al.* (LIGO Scientific and Virgo Collaborations), Observation of gravitational waves from a binary black hole merger, Phys. Rev. Lett. **116**, 061102 (2016).

[3] B. P. Abbott *et al.* (LIGO Scientific and Virgo Collaborations), GW170817: Observation of gravitational waves from a binary neutron star inspiral, Phys. Rev. Lett. **119**, 161101 (2017).

[4] R. Abbott *et al.* (LIGO Scientific, KAGRA, and Virgo Collaborations), Observation of gravitational waves from two neutron star–black hole coalescences, Astrophys. J. Lett. **915**, L5 (2021).

[5] F. Acernese *et al.* (Virgo Collaboration), Advanced Virgo: A second-generation interferometric gravitational wave detector, Classical Quantum Gravity **32**, 024001 (2015).

[6] B. P. Abbott *et al.* (LIGO Scientific and Virgo Collaborations), GWTC-1: A gravitational-wave transient catalog of compact binary mergers observed by LIGO and Virgo during the first and second observing runs, Phys. Rev. X **9**, 031040 (2019).

[7] R. Abbott *et al.* (LIGO Scientific and Virgo Collaborations), GWTC-2: Compact binary coalescences observed by LIGO and Virgo during the first half of the third observing run, Phys. Rev. X **11**, 021053 (2021).

[8] R. Abbott *et al.* (LIGO Scientific, Virgo, and KAGRA Collaborations), GWTC-3: Compact binary coalescences observed by LIGO and Virgo during the second part of the third observing run, Phys. Rev. X **13**, 041039 (2023).

[9] Chiara Caprini and Daniel G. Figueroa, Cosmological backgrounds of gravitational waves, Classical Quantum Gravity **35**, 163001 (2018).

[10] Nelson Christensen, Stochastic gravitational wave backgrounds, Rep. Prog. Phys. **82**, 016903 (2019).

[11] Mairi Sakellariadou, Gravitational waves: The theorist's Swiss knife, Universe **8**, 132 (2022).

[12] Vassiliki Kalogera *et al.*, Deeper, wider, sharper: Next-generation ground-based gravitational-wave observations of binary black holes, arXiv:1903.09220.

[13] Vicky Kalogera *et al.*, The next generation global gravitational wave observatory: The science book, arXiv:2111.06990.

[14] Matthew Evans *et al.*, A horizon study for cosmic explorer: Science, observatories, and community, arXiv:2109.09882.

[15] Matthew Evans *et al.*, Cosmic explorer: A submission to the NSF MPSAC ngGW subcommittee, arXiv:2306.13745.

[16] Ish Gupta *et al.*, Characterizing gravitational wave detector networks: From A# to cosmic explorer, arXiv:2307.10421.

[17] M. Punturo *et al.*, The Einstein Telescope: A third-generation gravitational wave observatory, Classical Quantum Gravity **27**, 194002 (2010).

[18] T. Regimbau, M. Evans, N. Christensen, E. Katsavounidis, B. Sathyaprakash, and S. Vitale, Digging deeper: Observing primordial gravitational waves below the binary black hole produced stochastic background, Phys. Rev. Lett. **118**, 151105 (2017).

[19] Michele Maggiore *et al.*, Science case for the Einstein Telescope, J. Cosmol. Astropart. Phys. 03 (2020) 050.

[20] Tania Regimbau, The astrophysical gravitational wave stochastic background, Res. Astron. Astrophys. **11**, 369 (2011).
[21] T. Regimbau and V. Mandic, Astrophysical sources of stochastic gravitational-wave background, Classical Quantum Gravity **25**, 184018 (2008).
[22] Alessandra Buonanno, Gunter Sigl, Georg G. Raffelt, Hans-Thomas Janka, and Ewald Muller, Stochastic gravitational wave background from cosmological supernovae, Phys. Rev. D **72**, 084001 (2005).
[23] Kamiel Janssens, Guillaume Boileau, Nelson Christensen, Francesca Badaracco, and Nick van Remortel, Impact of correlated seismic and correlated Newtonian noise on the Einstein Telescope, Phys. Rev. D **106**, 042008 (2022).
[24] Shichao Wu and Alexander H. Nitz, Mock data study for next-generation ground-based detectors: The performance loss of matched filtering due to correlated confusion noise, Phys. Rev. D **107**, 063022 (2023).
[25] Luca Reali, Andrea Antonelli, Roberto Cotesta, Ssohrab Borhanian, Mesut Çalışkan, Emanuele Berti, and B. S. Sathyaprakash, The impact of confusion noise on golden binary neutron-star events in next-generation terrestrial observatories, arXiv:2209.13452.
[26] Bei Zhou, Luca Reali, Emanuele Berti, Mesut Çalışkan, Cyril Creque-Sarbinowski, Marc Kamionkowski, and B. S. Sathyaprakash, Subtracting compact binary foregrounds to search for subdominant gravitational-wave backgrounds in next-generation ground-based observatories, Phys. Rev. D **108**, 064040 (2023).
[27] Bei Zhou, Luca Reali, Emanuele Berti, Mesut Çalışkan, Cyril Creque-Sarbinowski, Marc Kamionkowski, and B. S. Sathyaprakash, Compact binary foreground subtraction in next-generation ground-based observatories, arXiv:2209.01221.
[28] Ashish Sharma and Jan Harms, Searching for cosmological gravitational-wave backgrounds with third-generation detectors in the presence of an astrophysical foreground, Phys. Rev. D **102**, 063009 (2020).
[29] Haowen Zhong, Rich Ormiston, and Vuk Mandic, Detecting cosmological gravitational wave background after removal of compact binary coalescences in future gravitational wave detectors, Phys. Rev. D **107**, 064048 (2023).
[30] Surabhi Sachdev, Tania Regimbau, and B. S. Sathyaprakash, Subtracting compact binary foreground sources to reveal primordial gravitational-wave backgrounds, Phys. Rev. D **102**, 024051 (2020).
[31] Tania Regimbau, The quest for the astrophysical gravitational-wave background with terrestrial detectors, Symmetry **14**, 270 (2022).
[32] Benjamin P. Abbott *et al.* (LIGO Scientific and Virgo Collaborations), Upper limits on the stochastic gravitational-wave background from Advanced LIGO's first observing run, Phys. Rev. Lett. **118**, 121101 (2017); **119**, 029901(E) (2017).
[33] B. P. Abbott *et al.* (LIGO Scientific and Virgo Collaborations), Search for the isotropic stochastic background using data from Advanced LIGO's second observing run, Phys. Rev. D **100**, 061101 (2019).
[34] R. Abbott *et al.* (KAGRA, Virgo, and LIGO Scientific Collaboration), Upper limits on the isotropic gravitational-wave background from Advanced LIGO and Advanced Virgo's third observing run, Phys. Rev. D **104**, 022004 (2021).
[35] N. Aghanim *et al.* (Planck Collaboration), Planck 2018 results. VI. Cosmological parameters, Astron. Astrophys. **641**, A6 (2020); **652**, C4(E) (2021).
[36] Zhen Pan and Huan Yang, Improving the detection sensitivity to primordial stochastic gravitational waves with reduced astrophysical foregrounds, Phys. Rev. D **107**, 123036 (2023).
[37] C. Wu, V. Mandic, and T. Regimbau, Accessibility of the gravitational-wave background due to binary coalescences to second and third generation gravitational-wave detectors, Phys. Rev. D **85**, 104024 (2012).
[38] Xing-Jiang Zhu, Eric J. Howell, David G. Blair, and Zong-Hong Zhu, On the gravitational wave background from compact binary coalescences in the band of ground-based interferometers, Mon. Not. R. Astron. Soc. **431**, 882 (2013).
[39] Joseph D. Romano and Neil J. Cornish, Detection methods for stochastic gravitational-wave backgrounds: A unified treatment, Living Rev. Relativity **20**, 2 (2017).
[40] Valeria Ferrari, Sabino Matarrese, and Raffaella Schneider, Stochastic background of gravitational waves generated by a cosmological population of young, rapidly rotating neutron stars, Mon. Not. R. Astron. Soc. **303**, 258 (1999).
[41] Michal Dominik, Emanuele Berti, Richard O'Shaughnessy, Ilya Mandel, Krzysztof Belczynski, Christopher Fryer, Daniel E. Holz, Tomasz Bulik, and Francesco Pannarale, Double compact objects III: Gravitational wave detection rates, Astrophys. J. **806**, 263 (2015).
[42] E. S. Phinney, A practical theorem on gravitational wave backgrounds, arXiv:astro-ph/0108028.
[43] Mohammadtaher Safarzadeh, Sylvia Biscoveanu, and Abraham Loeb, Constraining the delay time distribution of compact binary objects from the stochastic gravitational wave background searches, Astrophys. J. **901**, 137 (2020).
[44] R. Abbott *et al.* (KAGRA, Virgo, and LIGO Scientific Collaborations), Population of merging compact binaries inferred using gravitational waves through GWTC-3, Phys. Rev. X **13**, 011048 (2023).
[45] Amanda M. Farah, Maya Fishbach, Reed Essick, Daniel E. Holz, and Shanika Galaudage, Bridging the gap: Categorizing gravitational-wave events at the transition between neutron stars and black holes, Astrophys. J. **931**, 108 (2022).
[46] Maya Fishbach, Reed Essick, and Daniel E. Holz, Does matter matter? Using the mass distribution to distinguish neutron stars and black holes, Astrophys. J. Lett. **899**, L8 (2020).
[47] Sylvia Biscoveanu, Philippe Landry, and Salvatore Vitale, Population properties and multimessenger prospects of neutron star–black hole mergers following GWTC-3, Mon. Not. R. Astron. Soc. **518**, 5298 (2022).
[48] Nicholas Farro w, Xing-Jiang Zhu, and Eric Thrane, The mass distribution of Galactic double neutron stars, Astrophys. J. **876**, 18 (2019).
[49] Philippe Landry and Jocelyn S. Read, The mass distribution of neutron stars in gravitational-wave binaries, Astrophys. J. Lett. **921**, L25 (2021).
[50] Piero Madau and Tassos Fragos, Radiation backgrounds at cosmic dawn: X-rays from compact binaries, Astrophys. J. **840**, 39 (2017).

[51] E. Vangioni, K. A. Olive, T. Prestegard, J. Silk, P. Petitjean, and V. Mandic, The impact of star formation and gamma-ray burst rates at high redshift on cosmic chemical evolution and reionization, Mon. Not. R. Astron. Soc. **447**, 2575 (2015).
[52] David W. Hogg, Distance measures in cosmology, arXiv: astro-ph/9905116.
[53] Tsvi Piran, The implications of the Compton (GRO) observations for cosmological gamma-ray bursts, Astrophys. J. Lett. **389**, L45 (1992).
[54] H. Sana, S. E. de Mink, A. de Koter, N. Langer, C. J. Evans, M. Gieles, E. Gosset, R. G. Izzard, J. B. Le Bouquin, and F. R. N. Schneider, Binary interaction dominates the evolution of massive stars, Science **337**, 444 (2012).
[55] Maya Fishbach and Vicky Kalogera, The time delay distribution and formation metallicity of LIGO-Virgo's binary black holes, Astrophys. J. Lett. **914**, L30 (2021).
[56] Paz Beniamini and Tsvi Piran, The gravitational waves merger time distribution of binary neutron star systems, Mon. Not. R. Astron. Soc. **487**, 4847 (2019).
[57] Michael Zevin, Anya E. Nugent, Susmita Adhikari, Wen-fai Fong, Daniel E. Holz, and Luke Zoltan Kelley, Observational inference on the delay time distribution of short gamma-ray bursts, Astrophys. J. Lett. **940**, L18 (2022).
[58] Tania Regimbau *et al.*, A mock data challenge for the Einstein Gravitational-Wave Telescope, Phys. Rev. D **86**, 122001 (2012).
[59] Krzysztof Belczynski and Vassiliki Kalogera, A New formation channel for double neutron stars without recycling: Implications for gravitational wave detection, Astrophys. J. Lett. **550**, L183 (2001).
[60] Krzysztof Belczynski, Rosalba Perna, Tomasz Bulik, Vassiliki Kalogera, Natalia Ivanova, and Donald Q. Lamb, A study of compact object mergers as short gamma-ray burst progenitors, Astrophys. J. **648**, 1110 (2006).
[61] Edo Berger *et al.*, A new population of high redshift short-duration gamma-ray bursts, Astrophys. J. **664**, 1000 (2007).
[62] Thomas Callister, Maya Fishbach, Daniel Holz, and Will Farr, Shouts and murmurs: Combining individual gravitational-wave sources with the stochastic background to measure the history of binary black hole mergers, Astrophys. J. Lett. **896**, L32 (2020).
[63] LIGO Document T2000100-v6, Technical Report.
[64] Maya Fishbach and Daniel E. Holz, Where are LIGO's big black holes? Astrophys. J. Lett. **851**, L25 (2017).
[65] Maya Fishbach and Daniel E. Holz, Picky partners: The pairing of component masses in binary black hole mergers, Astrophys. J. Lett. **891**, L27 (2020).
[66] B. P. Abbott *et al.* (LIGO Scientific and Virgo Collaborations), GW190425: Observation of a compact binary coalescence with total mass $\sim 3.4 M_{\odot}$, Astrophys. J. Lett. **892**, L3 (2020).
[67] Isobel M. Romero-Shaw, Nicholas Farrow, Simon Stevenson, Eric Thrane, and Xing-Jiang Zhu, On the origin of GW190425, Mon. Not. R. Astron. Soc. **496**, L64 (2020).
[68] Ssohrab Borhanian, GWBENCH: A novel Fisher information package for gravitational-wave benchmarking, Classical Quantum Gravity **38**, 175014 (2021).
[69] P. Fritschel, K. Kuns, J. Driggers, A. Effler, B. Lantz, D. Ottaway, S. Ballmer, K. Dooley, R. Adhikari, M. Evans, B. Farr, G. Gonzalez, P. Schmidt, and S. Raja, Report from the LSC Post-O5 Study Group, LIGO Technical Report T2200287, 2022.
[70] M. Branchesi *et al.*, Science with the Einstein Telescope: a comparison of different designs, J. Cosmol. Astropart. Phys. 07 (2023) 068.
[71] Bruce Allen and Joseph D. Romano, Detecting a stochastic background of gravitational radiation: Signal processing strategies and sensitivities, Phys. Rev. D **59**, 102001 (1999).
[72] Eric Thrane and Joseph D. Romano, Sensitivity curves for searches for gravitational-wave backgrounds, Phys. Rev. D **88**, 124032 (2013).
[73] Tania Regimbau, Duncan Meacher, and Michael Coughlin, Second Einstein Telescope mock science challenge: Detection of the gravitational-wave stochastic background from compact binary coalescences, Phys. Rev. D **89**, 084046 (2014).
[74] Duncan Meacher, Michael Coughlin, Sean Morris, Tania Regimbau, Nelson Christensen, Shivaraj Kandhasamy, Vuk Mandic, Joseph D. Romano, and Eric Thrane, Mock data and science challenge for detecting an astrophysical stochastic gravitational-wave background with Advanced LIGO and Advanced Virgo, Phys. Rev. D **92**, 063002 (2015).
[75] Sascha Husa, Sebastian Khan, Mark Hannam, Michael Pürrer, Frank Ohme, Xisco Jiménez Forteza, and Alejandro Bohé, Frequency-domain gravitational waves from nonprecessing black-hole binaries. I. New numerical waveforms and anatomy of the signal, Phys. Rev. D **93**, 044006 (2016).
[76] Sebastian Khan, Sascha Husa, Mark Hannam, Frank Ohme, Michael Pürrer, Xisco Jiménez Forteza, and Alejandro Bohé, Frequency-domain gravitational waves from nonprecessing black-hole binaries. II. A phenomenological model for the advanced detector era, Phys. Rev. D **93**, 044007 (2016).
[77] C. J. Moore, R. H. Cole, and C. P. L. Berry, Gravitational-wave sensitivity curves, Classical Quantum Gravity **32**, 015014 (2015).
[78] Maya Fishbach, Will M. Farr, and Daniel E. Holz, The most massive binary black hole detections and the identification of population outliers, Astrophys. J. Lett. **891**, L31 (2020).
[79] Maya Fishbach, Daniel E. Holz, and Will M. Farr, Does the black hole merger rate evolve with redshift?, Astrophys. J. Lett. **863**, L41 (2018).
[80] Ken'ichi Saikawa, A review of gravitational waves from cosmic domain walls," Universe **3**, 40 (2017).
[81] Alba Romero, Katarina Martinovic, Thomas A. Callister, Huai-Ke Guo, Mario Martínez, Mairi Sakellariadou, Feng-Wei Yang, and Yue Zhao, Implications for first-order cosmological phase transitions from the third LIGO-Virgo observing run, Phys. Rev. Lett. **126**, 151301 (2021).
[82] Jose R. Espinosa, Thomas Konstandin, Jose M. No, and Geraldine Servant, Energy budget of cosmological first-order phase transitions, J. Cosmol. Astropart. Phys. 06 (2010) 028.

[83] Daniel G. Figueroa and Erwin H. Tanin, Ability of LIGO and LISA to probe the equation of state of the early Universe, J. Cosmol. Astropart. Phys. 08 (2019) 011.
[84] Richard Easther, John T. Giblin, Jr., and Eugene A. Lim, Gravitational wave production at the end of inflation, Phys. Rev. Lett. **99**, 221301 (2007).
[85] R. Abbott *et al.* (LIGO Scientific, Virgo, and KAGRA Collaborations), Constraints on cosmic strings using data from the third Advanced LIGO–Virgo observing run, Phys. Rev. Lett. **126**, 241102 (2021).
[86] Alexander C. Jenkins, Richard O'Shaughnessy, Mairi Sakellariadou, and Daniel Wysocki, Anisotropies in the astrophysical gravitational-wave background: The impact of black hole distributions, Phys. Rev. Lett. **122**, 111101 (2019).
[87] Reed Essick, Amanda Farah, Shanika Galaudage, Colm Talbot, Maya Fishbach, Eric Thrane, and Daniel E. Holz, Probing extremal gravitational-wave events with coarse-grained likelihoods, Astrophys. J. **926**, 34 (2022).
[88] Katarina Martinovic, Patrick M. Meyers, Mairi Sakellariadou, and Nelson Christensen, Simultaneous estimation of astrophysical and cosmological stochastic gravitational-wave backgrounds with terrestrial detectors, Phys. Rev. D **103**, 043023 (2021).
[89] Wang-Wei Yu and Shao-Jiang Wang, Searching for double-peak and doubly-broken gravitational-wave spectra from Advanced LIGO-Virgo's first three observing runs, Phys. Rev. D **108**, 063526 (2023).
[90] Andrew R. Kaiser, Nihan S. Pol, Maura A. McLaughlin, Siyuan Chen, Jeffrey S. Hazboun, Luke Zoltan Kelley, Joseph Simon, Stephen R. Taylor, Sarah J. Vigeland, and Caitlin A. Witt, Disentangling multiple stochastic gravitational wave background sources in PTA data sets, Astrophys. J. **938**, 115 (2022).
[91] Thomas Callister, Letizia Sammut, Shi Qiu, Ilya Mandel, and Eric Thrane, The limits of astrophysics with gravitational-wave backgrounds, Phys. Rev. X **6**, 031018 (2016).
[92] Suvodip Mukherjee, Matthew S. P. Meinema, and Joseph Silk, Prospects of discovering subsolar primordial black holes using the stochastic gravitational wave background from third-generation detectors, Mon. Not. R. Astron. Soc. **510**, 6218 (2022).
[93] Rory Smith and Eric Thrane, Optimal search for an astrophysical gravitational-wave background, Phys. Rev. X **8**, 021019 (2018).
[94] Rory J. E. Smith, Colm Talbot, Francisco Hernandez Vivanco, and Eric Thrane, Inferring the population properties of binary black holes from unresolved gravitational waves, Mon. Not. R. Astron. Soc. **496**, 3281 (2020).
[95] Colm Talbot, Eric Thrane, Sylvia Biscoveanu, and Rory Smith, Inference with finite time series: Observing the gravitational Universe through windows, Phys. Rev. Res. **3**, 043049 (2021).
[96] Sharan Banagiri, Vuk Mandic, Claudia Scarlata, and Kate Z. Yang, Measuring angular N-point correlations of binary black hole merger gravitational-wave events with hierarchical Bayesian inference, Phys. Rev. D **102**, 063007 (2020).
[97] Sylvia Biscoveanu, Colm Talbot, Eric Thrane, and Rory Smith, Measuring the primordial gravitational-wave background in the presence of astrophysical foregrounds, Phys. Rev. Lett. **125**, 241101 (2020).
[98] Steven L. Finkelstein *et al.*, CEERS key paper. I. An early look into the first 500 myr of galaxy formation with JWST, Astrophys. J. Lett. **946**, L13 (2023).
[99] Yuichi Harikane, Masami Ouchi, Masamune Oguri, Yoshiaki Ono, Kimihiko Nakajima, Yuki Isobe, Hiroya Umeda, Ken Mawatari, and Yechi Zhang, A comprehensive study of galaxies at $z \sim 9$–16 found in the early JWST data: Ultraviolet luminosity functions and cosmic star formation history at the pre-reionization epoch, Astrophys. J. Suppl. Ser. **265**, 5 (2023).
[100] Leonard Lehoucq, Irina Dvorkin, Rahul Srinivasan, Clement Pellouin, and Astrid Lamberts, Astrophysical uncertainties in the gravitational-wave background from stellar-mass compact binary mergers, Mon. Not. R. Astron. Soc. **526**, 4378 (2023).
[101] C. Périgois, C. Belczynski, T. Bulik, and T. Regimbau, StarTrack predictions of the stochastic gravitational-wave background from compact binary mergers, Phys. Rev. D **103**, 043002 (2021).
[102] I. Kowalska-Leszczynska, T. Regimbau, T. Bulik, M. Dominik, and K. Belczynski, Effect of metallicity on the gravitational-wave signal from the cosmological population of compact binary coalescences, Astron. Astrophys. **574**, A58 (2015).
[103] Katarina Martinovic, Carole Perigois, Tania Regimbau, and Mairi Sakellariadou, Footprints of population III stars in the gravitational-wave background, Astrophys. J. **940**, 29 (2022).
[104] Ken Nakazato, Yuu Niino, and Norichika Sago, Gravitational-wave background from binary mergers and metallicity evolution of galaxies, Astrophys. J. **832**, 146 (2016).
[105] Irina Dvorkin, Elisabeth Vangioni, Joseph Silk, Jean-Philippe Uzan, and Keith A. Olive, Metallicity-constrained merger rates of binary black holes and the stochastic gravitational wave background, Mon. Not. R. Astron. Soc. **461**, 3877 (2016).
[106] I. Kowalska, T. Bulik, and K. Belczynski, Gravitational wave background from population III binaries, Astron. Astrophys. **541**, A120 (2012).
[107] Nikolaos Kouvatsos and Mairi Sakellariadou, The impact of population III stars on the astrophysical gravitational-wave background," arXiv:2404.05653.
[108] Ken K. Y. Ng, Salvatore Vitale, Will M. Farr, and Carl L. Rodriguez, Probing multiple populations of compact binaries with third-generation gravitational-wave detectors, Astrophys. J. Lett. **913**, L5 (2021).